Catalysis Today 299 (2018) 146–153

Contents lists available at ScienceDirect

Catalysis Today

journal homepage: www.elsevier.com/locate/cattod

Structure and reactivity of Pt–In intermetallic alloy nanoparticles: Highly selective catalysts for ethane dehydrogenation

Evan C. Wegener[a], Zhenwei Wu[a], Han-Ting Tseng[a], James R. Gallagher[b], Yang Ren[c], Rosa E. Diaz[d], Fabio H. Ribeiro[a], Jeffrey T. Miller[a,*]

[a] Davidson School of Chemical Engineering, Purdue University, 480 Stadium Mall Drive, West Lafayette, IN 47907-2100, USA
[b] Division of Chemical Sciences and Engineering, Argonne National Laboratory, 9700 S. Cass Avenue, Argonne, IL 60439, USA
[c] X-ray Science Division, Argonne National Laboratory, 9700 S. Cass Avenue, Argonne, IL 60439, USA
[d] Birck Nanotechnology Center, Purdue University, 1205 W. State Street, West Lafayette, IN 47907-2057, USA

ARTICLE INFO

Keywords:
PtIn nanoparticles
Ethane dehydrogenation
Synchrotron XRD of nanoparticles
EXAFS of PtIn bimetallic nanoparticles
Geometric effects in bimetallic alloys
Dehydrogenation selectivity

ABSTRACT

The structure of silica supported Pt and Pt–In bimetallic catalysts with nominal In:Pt atomic ratios of 0.7 and 1.4 were determined by in situ synchrotron XAS and XRD. It was seen that the addition of In led to the formation of two different intermetallic alloy phases. At an In:Pt ratio of 0.7 the Pt_3In phase with a Cu_3Au structure was formed. When the ratio was increased to 1.4 a shell of $PtIn_2$ having a CaF_2 structure formed around a core of Pt_3In. The catalysts were tested for ethane dehydrogenation at 600 °C to determine the effect of alloying on ethylene selectivity and turnover rate (TOR). The monometallic Pt catalysts was 73% selective for ethylene and had an initial TOR of 0.7 s^{-1}. Both alloy catalysts were ≈100% selective for dehydrogenation and had higher initial TOR, 2.8 s^{-1} and 1.6 s^{-1} for In:Pt ratio of 0.7 and 1.4, respectively. The increase in selectivity is attributed to the elimination of large Pt ensembles resulting from geometric changes to the catalyst surface upon alloying. Electronic changes due to the formation of Pt–In bonds are thought to be responsible for the increases in TOR in the alloy catalysts.

1. Introduction

The past decade has brought tremendous growth in the production of natural gas resulting from advancements in drilling technologies which have allowed for the recovery of gases trapped in shale formations. This increase in supply has made natural gas a viable feedstock for the production of chemicals and fuels. While predominately methane, shale deposits can contain up to 20% ethane and propane. These plentiful alkane resources can be directly converted by catalytic dehydrogenation to alkenes, valuable chemical building blocks. High purity products can be utilized in the polymer industry while mixtures can be converted to fuel range hydrocarbons [1].

Catalyst selectivity for dehydrogenation over hydrogenolysis, the primary competing reaction pathway, is paramount in light alkane dehydrogenation (LAD) processes. Industrially, Pt is used for LAD due to its intrinsic nature of favoring C–H bond activation over C–C bond activation [2]. The addition of Sn as a promoter results in higher olefin selectivity and catalyst stability [3–12]. The promotional effects have been attributed to the formation of Pt–Sn alloys [3,10–12]. Alloying can change the geometric and electronic properties of catalysts and both effects have been proposed to be the dominate factor responsible for improved selectivity and stability. For the geometric case it has been proposed that alloying with Sn eliminates large Pt ensembles responsible for hydrogenolysis and coke forming reactions while retaining catalytic activity for dehydrogenation [3–5]. The Pt_3Sn, PtSn, and $PtSn_2$ alloy phases have been identified in model Pt–Sn catalysts. However, because of the very small particles and low metal loadings the crystal phase of commercial catalysts has not been reported [13–17]. For the electronic case the formation of Pt–Sn bonds is thought to transfer electron density from Sn to Pt resulting in enhanced olefin desorption and improved selectivity [17–20].

Recently Pd–Zn bimetallic catalysts have been shown to be highly selective for propane dehydrogenation. The addition of Zn to Pd catalysts led to the formation of a 1:1 intermetallic alloy with a AuCu structure and resulted in an increase in propylene selectivity from 10% for monometallic Pd to 98% for the alloy [21,22]. Similar results have been reported for bimetallic Pd–In catalysts used for ethane dehydrogenation. A 1:1 PdIn intermetallic alloy with a CsCl structure was formed which led to an increase in ethylene selectivity from 53% to 98% [23]. In both studies the increase in olefin selectivity was

* Corresponding author.
E-mail address: mill1194@purdue.edu (J.T. Miller).

http://dx.doi.org/10.1016/j.cattod.2017.03.054
Received 14 October 2016; Received in revised form 8 March 2017; Accepted 27 March 2017
Available online 15 April 2017

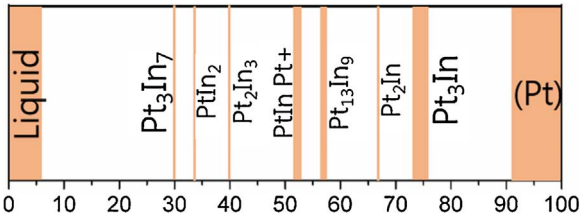

Fig. 1. Binary Pt–In phase diagram at 600 °C adapted from Okamoto [27].

attributed to the formation of the 1:1 alloy phase in which the active Pd atoms are geometrically isolated by inactive Zn or In. These works demonstrate that selective LAD catalysts can be made through the formation of certain intermetallic alloy structures.

The addition of In to Pt catalysts has also been shown to increase olefin selectivity for LAD [24] and to reduce activity for hydrogenolysis [25,26]. The changes in catalytic properties have been attributed to the formation of bimetallic Pt–In particles, but exact structures have not been determined. The binary phase diagram for Pt and In at 600 °C is shown in Fig. 1.

Pt and In can form seven intermetallic alloys. Unlike solid solutions where atoms occupy random lattice positions, atoms in intermetallic alloys sit in fixed sites which results in active sites with well-defined geometric and electronic properties [28]. Therefore, determination of the exact structure of bimetallic nanoparticles is crucial for understanding catalytic properties.

Here, we report on the synthesis, characterization, and catalytic performance of a monometallic Pt and two bimetallic Pt–In catalysts with different Pt:In atomic ratios supported on silica. The catalysts were characterized by CO chemisorption, scanning transmission electron microscopy (STEM), in situ X-ray absorption spectroscopy (XAS), and in situ X-ray diffraction (XRD). Ethane dehydrogenation was used to evaluate the effect of In on the olefin selectivity and reaction rate.

2. Experimental

2.1. Catalyst synthesis

Pt–In bimetallic catalysts (target loadings of 4 wt.% Pt and 3 and 6 wt.% In) were synthesized by sequential incipient wetness impregnation. The required amount of $In(NO_3)_3{\cdot}xH_2O$ (Sigma Aldrich) was dissolved in 8 mL of water. Citric acid (Sigma Aldrich) was added to the solution at a 3:1 molar ratio of citric acid to $In(NO_3)_3$. Approximately 5 mL of ammonium hydroxide solution (30%, Sigma Aldrich) was then added to the solution. Initially a white precipitate formed which dissolved upon further addition of ammonium hydroxide. The resulting solution (pH ≈ 11) was added dropwise to 15 g of Silica (Davisil 636 silica gel, Sigma Aldrich, 480 m^2/g surface area and 0.75 mL/g pore volume) with continuous stirring. The obtained catalysts were dried overnight at 125 °C and then calcined for 3 h at 600 °C. 0.48 g of $Pt(NH_3)_4(NO_3)_2$ was dissolved in a mixture of 3 mL of ammonium hydroxide solution and 3.5 mL of water. The resulting solution was added dropwise to 6 g of the In/SiO_2 precursor catalysts. The obtained catalysts were dried overnight at 125 °C and calcined at 225 °C for 3 h. The Pt–In catalysts were reduced at 250 °C for 30 min and then at 600 °C for 30 min in 5% H_2/N_2 at 100 cc/min.

For comparison a 2 wt.% monometallic Pt catalyst was synthesized by the strong electrostatic adsorption method (SEA). 5 g of silica was added to 50 mL of water. Ammonium hydroxide was added until the pH of the mixture was ≈11. 0.2 g of $Pt(NH_3)_4(NO_3)_2$ was dissolved in 25 mL of water and ammonium hydroxide solution was added until a pH ≈ 11. The Pt solution was added to the silica mixture with constant stirring. The obtained catalyst was filtered, washed with H_2O, filtered, and dried overnight at 125 °C. The catalyst was calcined at 300 °C for 3 h followed by reduction at 250 °C for 30 min and then 600 °C for 30 min in 5% H_2/N_2 at 100 cc/min.

2.2. Atomic absorption spectroscopy (AAS)

The indium content of the bimetallic catalysts after reduction at 600 °C was determined by AAS using a PerkinElmer AAnalyst 300 spectrometer. 3 mL of aqua regia was added to approximately 40 mg of sample and left overnight to dissolve. The solutions were then diluted with H_2O to be within the linear detection range of the instrument. The instrument was calibrated using an In AAS standard obtained from Sigma Aldrich. Metal loadings were obtained from the average values of two sets of dissolved samples, which differed by less than 5%.

2.3. CO chemisorption

Pt dispersions were measured by CO chemisorption using a Micromeritics ASAP 2020 chemisorption device. Approximately 0.1 g of catalyst was placed in a U-shaped quartz reactor. Before measurements the catalysts were reduced at 600 °C for 30 min in a flow of 5% H_2/He at 50 cc/min, cooled to 35 °C under vacuum, and then held under vacuum for 30 min. Measurements were conducted at 35 °C with the CO adsorption on Pt being determined from the difference between two repeat isotherms. A binding stoichiometry of 1:1 was assumed to calculate dispersion.

2.4. STEM

STEM images were acquired using the FEI Titan Scanning Transmission Electron Microscope (80–300 kV, 1 nm spatial resolution in STEM) at Birck Nanotechnology Center, Purdue University. Catalysts samples were ground to a fine powder and dispersed in isopropyl alcohol. The solutions were added dropwise onto ultrathin Carbon film-Au TEM ready grids (TedPella) and the solvent evaporated on a hot plate. Images were taken using the high angle annular dark field (HAADF) detector at 300 kV. 200 particles were counted to determine the size distribution for each sample using the ImageJ program.

2.5. In situ X-ray absorption spectroscopy (XAS)

XAS measurements at the Pt L_{III} edge (11.564 keV) and In K edge (27.940 keV) were taken at the bending magnet beamline of the Materials Research Collaborative Access Team (MR-CAT) at the Advanced Photon Source (APS), Argonne National Lab. Measurements were taken in step-scan transmission mode in about 10 min.

Samples were ground to a fine powder and pressed into a stainless-steel sample holder to form a self-supporting wafer. The sample holder was placed in a quartz tube with ports containing Kapton windows so samples could be treated prior to measurements. Samples were reduced in 100 cc/min of 3% H_2/He for 30 min at 600 °C. Following reduction, the samples were cooled to room temperature in 100 cc/min of He. Trace oxidants in He were removed by passing through a Matheson PUR-Gas Triple Purifier Cartridge. Spectra were obtained at room temperature in He.

WINXAS 3.1 software [29] was used to fit XAS data. The EXAFS coordination parameters were obtained by a least-squares fit in R-space of the k^2-weighted Fourier transform data from 3.0 to 12.0 $Å^{-1}$. The first shell fit of the magnitude and imaginary parts were performed between 1.8 and 2.9 Å at the Pt L_{III} edge and between 1.5 and 3.2 Å at the In K edge. Fits were performed by refinement of coordination numbers (CN), bond distances (R), and energy shift (E_o). $\Delta\sigma^2$ was kept constant for each sample and CN and R were allowed to vary to determine the correct fit. Phase and amplitude fitting functions for Pt–Pt were determined from Pt foil (CN = 12 at 2.77 Å) and FEFF calculations for Pt–In [30].

2.6. In situ X-ray diffraction (XRD)

XRD measurements were performed at the 11-ID-C beam line at the

APS, Argonne National Lab. Diffraction patterns were collected in transmission mode with a PerkinElmer large area detector using X-rays at 105.091 keV (λ = 0.11798 Å). Samples were ground to a fine powder, pressed into a thin wafer, and loaded into a Linkam Thermal Stage. Prior to measurements the stage was purged with Ar for 5 min at room temperature and then ramped to 600 °C in 3% H_2/Ar at 50 cc/min. Diffraction patterns (the summation of 30 exposures of 5 s each) were collected after reduction at 600 °C for 20 min. Samples were then cooled to room temperature in the same atmosphere and diffraction patterns collected. The empty sample stage and bare silica support were treated with the same procedure for background subtraction. The obtained 2-D diffraction patterns were integrated to 1-D intensity versus 2Θ plots using the Fit2D software [31]. MAUD (Materials Analysis Using Diffraction) was used to simulate theoretical diffraction patterns of potential Pt–In alloy phases which were used as standards to determine the crystal structure of each catalyst [32].

2.7. Ethane dehydrogenation kinetics

Ethane dehydrogenation kinetics were measured using a quartz fixed-bed reactor with 3/8-in. ID. A thermocouple was placed within a quartz thermocouple well positioned at the bottom center of the catalyst bed to measure the reaction temperature within the bed. Before testing the catalyst was reduced under 40 cc/min of 5% H_2/N_2 while the temperature was raised to 600 °C where it was held for 30 min. Catalysts were compared under two sets of conditions. To compare catalyst selectivity for ethylene the catalysts were tested at an initial conversion of 15% under a reaction atmosphere of 5% C_2H_6, 6% H_2, 49.3% N_2, balanced in He at a total flow rate of 150 cc/min and 600 °C. Turnover rates (TOR) were measured at 600 °C under a reaction atmosphere of 5% C_2H_6, 2% H_2, 0.5% C_2H_4, 49.3% N_2, balanced in He at a total flow rate of 150 cc/min. The approach to equilibrium was considered for the calculation of TOR following the work of Koryabkina et al. [33]. The rate expression used is,

$$\text{rate} = k_f [C_2H_6]^a [C_2H_4]^b [H_2]^c (1 - \beta);$$
$$\beta = [C_2H_4][H_2]/K[C_2H_6]$$

where k_f is the forward rate constant, K is the equilibrium constant, and β is the approach to equilibrium. The value of β was found to be less than 0.17 for all reactions indicating the reactions were far from equilibrium. Apparent activation energies were measured at four temperatures between 570 and 600 °C once the catalysts had stabilized at conversions below 10%.

3. Results

3.1. AAS

After the bimetallic catalysts were initially reduced at 600 °C, a yellow residue was observed at the outlet of the reactor tube. The yellow color, characteristic of In_2O_3 and identical to the color of the calcined, In impregnated SiO_2, suggests the residue is a result of a loss of In oxide from the catalyst. The actual In:Pt ratios in the reduced bimetallic catalysts were determined by AAS and are reported in Table 1.

Table 1
AAS, CO chemisorption, and STEM results.

Catalyst	Pt loading (wt.%)	In loading (wt.%)	In:Pt atomic ratio	Pt dispersion (%)	Particle size (nm)
Pt	2.0	/	/	29	3.5 ± 1.6
Pt–In(0.7)	4.0	1.7	0.7	13	3.0 ± 0.7
Pt–In(1.4)	4.0	3.2	1.4	9	3.4 ± 1.2

After high temperature reduction the In loadings of the two bimetallic catalysts were approximately half the nominal loading, resulting in catalysts with 1.7% and 3.2% In by weight. The two bimetallic catalysts were named for the reduced In:Pt atomic ratios determined from AAS, Pt–In(0.7) and Pt–In(1.4), respectively. The yellow residue was not seen after subsequent reductive pretreatments of the bimetallic catalysts indicating further loss of In was negligible.

3.2. CO chemisorption and STEM

CO chemisorption and STEM were used to determine platinum dispersions and particle size distributions of the three catalysts. The results are given in Table 1. The average particle size of the monometallic Pt catalyst is 3.5 nm, in agreement with what would be expected from the measured dispersion value of 29%. Pt–In(0.7) and Pt–In(1.4) were determined to have Pt dispersions of 13% and 9% respectively. The average particle sizes of the two bimetallic catalysts were found to be 3.0 nm and 3.4 nm, smaller than what would be expected from the measured dispersion values. The lower dispersion values for the bimetallic catalysts are likely from coverage of the nanoparticle surface by a species which does not adsorb CO, for example metallic In.

3.3. In situ XAS

XAS measurements were conducted at the Pt L_{III} (11.564 keV) and In K (27.940 keV) edges to determine the local coordination environments of Pt and In and determine whether bimetallic nanoparticles were formed in the Pt–In catalysts. Spectra were collected at room temperature in He after reduction at 600 °C. Pt L_{III} edge XANES of the Pt and Pt-In catalysts are shown in Fig. 2a and In K edge XANES of the Pt–In catalysts and an In_2O_3 reference are shown in Fig. 2b.

The XANES shape, white line intensity, and edge energy (11.5640 keV, Table 2) of the Pt catalyst are very similar to that of the Pt foil. The white line intensities of Pt–In(0.7) and Pt–In(1.4) are consistent with metallic Pt, but the edge energies have been shifter to higher energy, 11.5648 keV and 11.5651 keV, also given in Table 2. The change in the shape and energy of the XANES spectra of the Pt–In catalysts is consistent with the formation of bimetallic PtIn nanoparticles. Comparison of the Pt–In(0.7) and Pt–In(1.4) XANES spectra show differences in edge energy and position of the first peak in the white line suggesting the Pt in the two samples also have different coordination environments. The energy of the In XANES are 27.9402 keV, shifted to higher energy than metallic In (27.940 keV) and are given in Table 2. The decrease in the white line intensity of the spectra of the Pt–In catalysts compared to the In_2O_3 reference is indicative of a fraction of In being metallic. The Pt L_{III} and In K edge EXAFS of the catalysts after reduction at 600 °C are shown in Fig. 3.

The local structure, coordination numbers (CN) and bond distances (R), of the Pt and In were determined from the k^2-weighted first shell EXAFS spectra, and the results are in Table 2.

The Pt–Pt CN of 8.4 at a distance of 2.76 Å for the monometallic Pt catalyst are typical of 3 nm Pt nanoparticles, in agreement with chemisorption and STEM results [34]. The Pt–In catalysts cannot be fit with only Pt–Pt scattering and a good fit was obtained by adding a contribution for Pt–In scattering. Pt–In(0.7) has a Pt–In CN of 3.3 and a Pt–Pt CN of 5.7. Both Pt–In and Pt–Pt are at a distance of 2.79 Å, the latter is slightly longer than the Pt–Pt bonds in the monometallic Pt catalyst. The Pt–In coordination number in Pt–In(1.4) is 5.1, larger than that in Pt–In(0.7). However, the Pt–In bond distance of 2.74 Å is shorter than that of Pt–In(0.7). The increase in Pt–In coordination was accompanied by a decrease in the Pt–Pt CN to 4.4, but at the same bond distance, 2.79 Å, as Pt–In(0.7).

At the In edge, the bimetallic catalysts show a set of two peaks between 2 and 3 Å (phase uncorrected distance), typical of metal–metal scattering, and a shoulder around 1.8 Å (phase uncorrected distance),

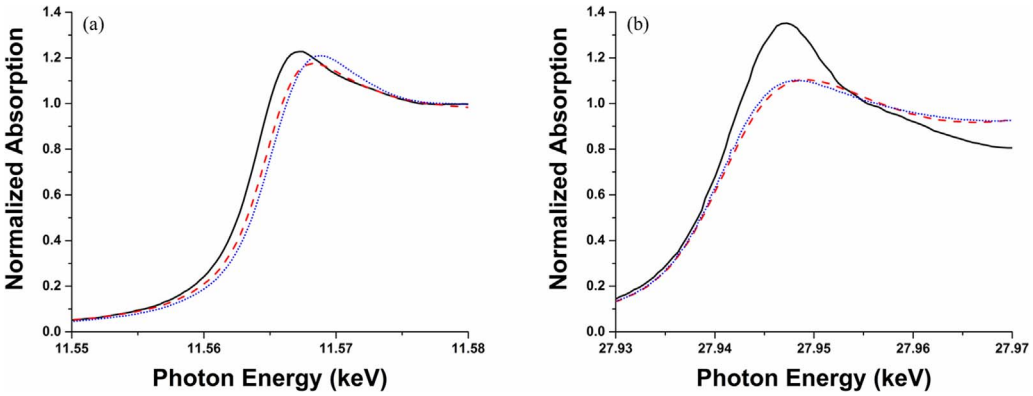

Fig. 2. XANES spectra of catalysts reduced at 600 °C (a) Pt L_{III} edge - Pt (black, solid), Pt-In(0.7) (red, dashed), and Pt-In(1.4) (blue, dotted) and (b) In K edge – In_2O_3 (black, solid), Pt-In (0.7) (red, dashed), and Pt-In(1.4) (blue, dotted). (For interpretation of the references to color in this figure legend, the reader is referred to the web version of this article.)

Table 2
XANES and EXAFS fitting parameters following reduction at 600 °C.

Catalyst	Edge	XANES energy (keV)	Scattering pair	CN	R (Å)	$\Delta\sigma^2 \times 10^3$	E_o (eV)
Pt	Pt	11.5640	Pt–Pt	8.4	2.76	2.0	−0.1
Pt–In(0.7)	Pt	11.5648	Pt–Pt	5.7	2.79	4.0	−6.0
			Pt–In	3.3	2.79	4.0	4.7
	In	27.9402	In–O	0.8	2.11	4.0	−8.2
			In–Pt	3.5	2.79	4.0	−1.2
Pt–In(1.4)	Pt	11.5651	Pt–Pt	4.4	2.79	4.0	−10.0
			Pt–In	5.1	2.74	4.0	2.9
	In	27.9402	In–O	0.7	2.14	4.0	−8.9
			In–Pt	2.9	2.74	4.0	−2.4
Pt foil	Pt	11.5640	Pt–Pt	12	2.77	0.0	−0.1

typical of In–O scattering. Pt–In(0.7) has an In–O CN of 0.8 at a distance of 2.11 Å and an In–Pt CN of 3.5 at a distance of 2.79 Å. Similar values of In–O CN and bond distance, 0.7 and 2.14 Å respectively, were present in Pt–In(1.4). Pt–In(1.4) was found to have a In–Pt CN of 2.9 at a distance of 2.74 Å, fewer In–Pt bonds at a shorter distance compared to Pt–In(0.7). The In–O scattering seen in both catalysts is a result of unreduced indium oxide on the catalyst. The In–O coordination numbers of 0.8 and 0.7 for Pt–In(0.7) and Pt–In(1.4) are lower than the In–O coordination number of 6 in bulk In_2O_3 and it can be estimated that approximately 90% of the In in each catalyst has been incorporated into the bimetallic particles. The In–O bond distances are in agreement with what has been reported for amorphous In_2O_3 [35]. No evidence of In–In scattering was seen in the EXAFS of either bimetallic catalyst. From XAS it is evident that bimetallic nanoparticles are formed in both Pt–In catalysts. However, XAS provides local structural information and does not determine whether a specific alloy phase or a disordered structure is formed.

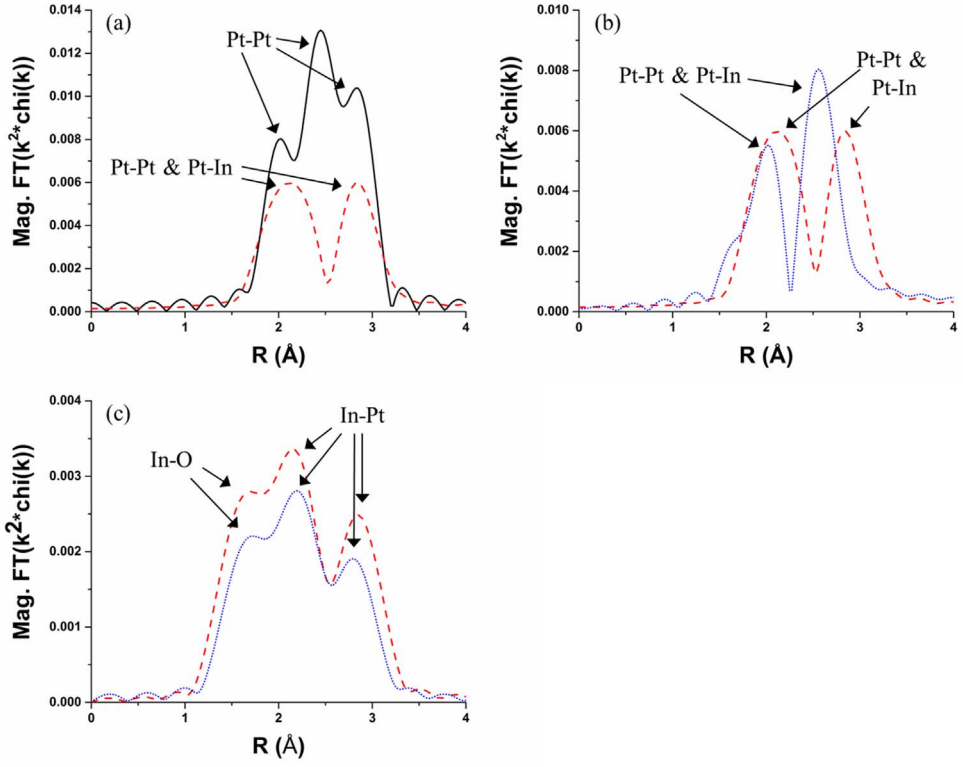

Fig. 3. EXAFS spectra of catalysts reduced at 600 °C (a) Pt L_{III} edge of – Pt (black, solid) and Pt–In(0.7) (red, dashed), (b) Pt L_{III} edge of - Pt-In(0.7) (red, dashed) and Pt-In(1.4) (blue, dotted), and (c) In K edge of – Pt-In(0.7) (red, dashed) and Pt-In(1.4) (blue, dotted). (For interpretation of the references to color in this figure legend, the reader is referred to the web version of this article.)

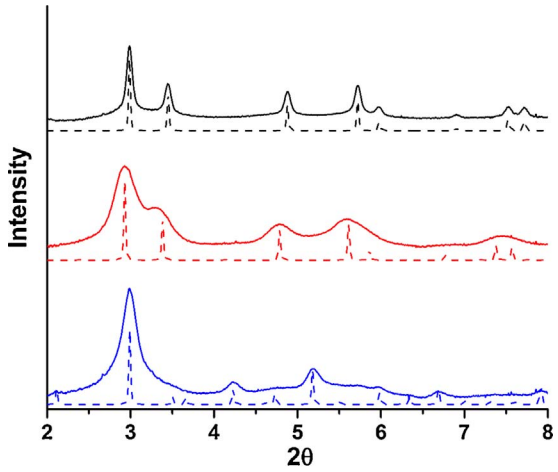

Fig. 4. Background subtracted XRD patterns of catalysts following reduction at 600 °C (Pt (black, top), Pt-In(0.7) (red, middle), and Pt-In(1.4) (blue, lower)) and simulated spectra of identified phases (Pt (black dashed, top), Pt_3In (red dashed, middle), and $PtIn_2$ (blue dashed, lower)). (For interpretation of the references to color in this figure legend, the reader is referred to the web version of this article.)

3.4. In situ XRD

To determine if the bimetallic Pt–In particles formed an ordered structure, in situ synchrotron XRD measurements were performed. Due to their small size a high fraction of the atoms are at the surface and are oxidized in air. Therefore, to obtain meaningful structural information the data has to be collected in situ [36]. Diffraction patterns were collected at 600 °C after reduction and then after cooling to room temperature. Aside from peak displacement due to thermally induced lattice expansion, the diffraction patterns were identical indicating the same crystal structure present at 600 °C and room temperature. To identify the phases present, the room temperature spectra were compared to simulated diffraction patterns of known Pt–In alloys. The diffraction pattern of the isolated nanoparticles in each catalyst and the simulated pattern of the identified phases are shown in Fig. 4. The patterns were obtained by subtracting the scattering due to the silica support, the empty cell, and gases present in the X-ray path from the full diffraction patterns. The energy of the synchrotron X-rays was 105.091 keV, much higher than Cu Kα radiation (8.0463 keV) which is typically used in lab-based instruments. Thus, the diffraction peaks occur at much lower angles in the synchrotron XRD patterns. The weak and broad diffraction peaks result from the low metal loading and small size of the nanoparticles.

The diffraction pattern from the monometallic catalyst is characteristic of FCC Pt with peaks from the (111) and (200) reflections at 2.99° and 3.45°. The average lattice parameter calculated from Bragg's law and the position of the (111) and (200) reflections is 3.92 Å which corresponds to a Pt–Pt bond distance of 2.77 Å and is consistent with EXAFS results. Pt–In(0.7) has a diffraction pattern similar to FCC Pt, however, all the peaks are shifted to lower angles indicating an increase in the size of the unit cell. The diffraction pattern of Pt–In(0.7) matches that of the Pt_3In alloy with a Cu_3Au structure with the most intense peaks at 2.93° and 3.33° corresponding to the (111) and (200) reflections. The diffraction pattern of Pt–In(1.4) is distinctly different from the other two catalysts. There is one main peak in the diffraction pattern centered at 2.99° which has been identified as the (220) reflection of the $PtIn_2$ alloy with a CaF_2 structure. However, all the peaks present are shifted to lower angle by 0.01–0.02°, indicating a larger unit cell than the ideal structure.

3.5. Ethane dehydrogenation kinetics

Initial turnover rates and selectivity of ethane dehydrogenation were determined at 600 °C at 15% conversion using a reaction mixture of 5% ethane and 6% H_2 balanced in inert. The results are given in Table 3. Selectivity was calculated from the observed gas phase products (ethylene from dehydrogenation and methane from hydrogenolysis). The small amount of coke on the catalyst was not included. Alloy formation led to increased ethylene selectivity and stability. The Pt catalyst was 73% selective for ethylene and deactivated after 1 h to a constant conversion of 9% with selectivity improving to 91% as the catalyst deactivated. Pt–In(0.7) and Pt–In(1.4) exhibited high ethylene selectivities of 99% and 98% with little deactivation in 5 h. The In impregnated silica was tested under the same conditions and showed negligible conversion.

Table 3
Catalytic results for ethane dehydrogenation reactions.

Catalyst	$C_2H_6 + H_2$		$C_2H_6 + C_2H_4 + H_2$		
	Initial selectivity	Initial TOR[a] (s^{-1})	Initial TOR[a] (s^{-1})	Steady state TOR[a] (s^{-1})	E_{app} (kJ/mol)
Pt	73%	1.8	0.7	0.2	76
Pt–In(0.7)	99%	5.3	2.8	1.0	95
Pt–In(1.4)	98%	1.9	1.6	1.0	137

[a] Per mole of surface Pt as measured by CO chemisorption.

Turnover rates (TOR) and apparent activation energies (E_{app}) were determined with a reaction gas of 0.5% ethylene with 5% ethane and 2% H_2. Results are also shown in Table 3. The initial TOR and steady state TOR were higher on the alloy catalysts than the monometallic Pt catalyst. The initial TOR of the Pt catalyst was 0.7 s^{-1} and deactivated to a steady-state value of 0.2 s^{-1}. Pt–In(0.7) had the highest initial TOR of the three catalysts, 2.8 s^{-1}, while Pt–In(1.4) had an initial TOR of 1.6 s^{-1}. The Pt–In catalysts had equivalent steady state TOR of 1.0 s^{-1}. The addition of ethylene to the feed decreased the initial TORs of Pt and Pt–In(0.7) while the TOR of Pt–In(1.4) was almost unchanged. Alloy formation also led to increases in the apparent activation energy. The addition of In led to an increase in E_{app} from 76 kJ/mol for Pt to 95 kJ/mol for Pt–In(0.7) and 137 kJ/mol for Pt–In(1.4). The increase in TOR and higher E_{app} in the Pt–In catalysts are consistent with an electronic promotion of Pt by In. Differences in the TOR and E_{app} of the two Pt-In catalysts also suggests that there is a different In promotional effect due to the different Pt–In alloy structures.

4. Discussion

The addition of In to the Pt catalyst led to the formation of multiple Pt–In intermetallic alloy phases. The catalyst synthesized with a bulk In:Pt atomic ratio of 0.7 formed the Pt_3In phase with a Cu_3Au structure. Pt_3In has the same structure as the Pt_3Sn alloy which has been reported for Pt–Sn bimetallic catalysts [14–17]. The Pt–In and Pt–Pt bond distances of 2.79 Å seen by EXAFS is in agreement with the bond distances in the ideal Pt_3In structure of 2.82 Å. Increasing the In:Pt ratio to 1.4 led to the formation of a second alloy phase, $PtIn_2$ with a CaF_2 structure. $PtSn_2$ alloys of equivalent structure have been reported to be selective for alkane dehydrogenation [13,14]. The Pt–In bond distance in the ideal $PtIn_2$ structure is 2.76 Å, similar to the distance seen by EXAFS, 2.74 Å. However, there is still Pt–Pt scattering in the EXAFS spectra of the Pt–In(1.4) catalysts. In the ideal $PtIn_2$ structure Pt has only In first nearest neighbors; therefore, the Pt–Pt scattering indicates a second phase is also present. The AAS results provide further evidence since the measured In:Pt ratio is 1.4, less than the minimum ratio necessary to form a complete alloy of the correct stoichiometric ratio of 2:1. The Pt–Pt bond distance determined by EXAFS is 2.79 Å, the same as was seen in the Pt–In(0.7) catalyst indicating the second phase present is likely Pt_3In. It has been reported for Pd–Zn intermetallic alloy catalysts that alloy formation occurs first on the surface of Pd nanoparticles and progresses toward the center suggesting that the

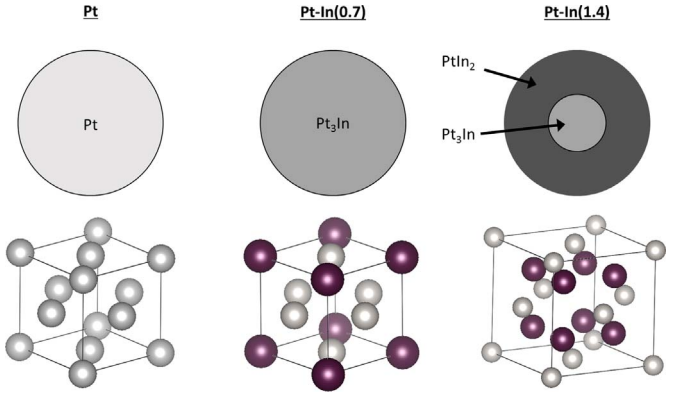

Fig. 5. Schematic of geometric structure of Pt and Pt–In catalysts and crystal structures of the active phase (Pt – light atoms and In – dark atoms.) [37,38].

promoter metal diffuses into the Pd nanoparticles as more ZnO is reduced to metal at higher temperatures [21,22]. Based on these observations it is likely that for the Pt–In(1.4) catalyst as more In_2O_3 is reduced it forms a shell of $PtIn_2$ around a core of Pt_3In. Fig. 5 shows the evolution of nanoparticle structure with increasing In:Pt ratio and the unit cells of the alloy phases identified.

Initial addition of In leads to the formation of the Pt_3In phase and continued addition leads to the formation of the $PtIn_2$ phase at the surface of the Pt_3In nanoparticles. Due to the limiting amount of In present in the Pt–In(1.4) catalyst, a shell of $PtIn_2$ is formed around a core of the Pt_3In phase.

The alloy phases formed in the Pt-In catalysts have different stoichiometry's and structures than those which have been reported to form in highly selective Pd–Zn and Pd–In dehydrogenation catalysts, which both form alloys with atomic ratios of 1:1 having a AuCu and a CsCl structure, respectively [21–23]. While the bulk phase diagrams show multiple intermetallic alloy phases over the composition ranges studied, only the 1:1 alloys were formed in the Pd–Zn and Pd–In catalysts [39,40]. For Pd–In it was also proposed that alloy formation was kinetically controlled and that the 1:1 alloy was selectively formed due to its similar crystal structure to FCC Pd. Similar phenomena occurs in the Pt–In catalysts. The structures of the Pt–In intermetallic alloys that were not formed in the Pt–In catalysts are shown in Fig. 6.

The phases formed, Pt_3In and $PtIn_2$, have crystal structures which can be formed by minimal rearrangement of the Pt atoms in the initially reduced FCC structure. The structures in Fig. 6 require significant reordering of the Pt and In atoms and are not formed. The observed structures suggest that alloy formation is kinetically, rather than thermodynamically controlled, consistent with previous studies on PdZn and PdIn bimetallic nanoparticles. Thus, all compositionally possible structures are not formed.

Although the 1:1 alloys were the only phases formed in the PdZn and PdIn catalysts, the structure of equivalent stoichiometry was not observed in the present work. The unit cell of the PdZn 1:1 alloy is body-centered tetragonal while that of PdIn is body-centered cubic, both similar in structure to FCC Pd. As seen in Fig. 6, the 1:1 PtIn alloy has a monoclinic unit cell very different in structure from FCC Pt. This large difference in crystal structure is believed to be responsible for the 1:1 PtIn phase not forming even though alloys with the same stoichiometry were formed in the PdZn and PdIn bimetallic catalysts.

The observed changes in crystal structure coincide with changes in the ethane dehydrogenation performance of each catalyst. The monometallic Pt catalyst exhibited a moderate selectivity of 73% at 15% conversion and deactivated quickly, behavior typical of Pt catalysts [3,22]. Ethylene selectivities of nearly 100% were achieved over the alloy catalysts which also showed more stable performance than monometallic Pt. Alloy formation also increased dehydrogenation TORs. The Pt_3In phase present in Pt–In(0.7) had the highest initial TOR of the three catalysts, almost 4 times that of the monometallic Pt catalyst. Increased In content and formation of the $PtIn_2$ phase in Pt–In (1.4) resulted in a lower initial TOR than Pt–In(0.7), but still higher than that measured for Pt. Similar behavior was seen by Sun et al., where bimetallic Pt–In nanoparticles were confirmed by EXAFS; however the exact structure was not determined. It was reported that the addition of In and formation of bimetallic particles increased the ethylene selectivity from 60% for monometallic Pt to greater than 96% for all the Pt–In catalysts. The TOR increased from 0.7 s^{-1} for Pt with increasing In:Pt ratios before reaching a maximum of 1.6 s^{-1} at a ratio of 1.7 and decreasing to 0.5 s^{-1} with further addition of In [24]. Pt–In(0.7) and Pt–In(1.4) had equivalent steady state TOR, approximately five times that of monometallic Pt.

The increase in selectivity for dehydrogenation of the alloy catalysts compared to the monometallic catalyst can be attributed to the elimination of large Pt ensembles upon alloy formation, i.e. a geometric effect. Dehydrogenation is a structure insensitive reaction requiring a single active atom [46,47] while hydrogenolysis is a structure sensitive reaction requiring an ensemble of active atoms [47]. It has been shown that Pt 3-fold hollow sites present in large Pt ensembles are responsible for the formation of strongly adsorbed alkylidyne species which are precursors of hydrogenolysis and coke forming reactions [48–51]. The formation of Pt_3In reduces the number of Pt 3-fold hollow sites and it has been shown that the formation of ethylidyne is suppressed on Pt_3Sn alloys with equivalent structures to the Pt_3In phase in Pt–In(0.7) [48,50,51]. While the number of Pt 3-fold hollow sites is reduced, they are not completely eliminated, and trimers of Pt atoms are still present in the alloy structure. However, the Pt–Pt bond distance of 2.82 Å is slightly elongated from 2.77 Å, the Pt–Pt bond distance in FCC Pt. It has been proposed that two adjacent active atoms are required for hydrogenolysis reactions [52–54]. Although Pt–In(0.7) contains three adjacent Pt atoms it is highly selective for dehydrogenation suggesting that C–C bond cleavage requires ensembles of more than three active atoms. In the $PtIn_2$ phase, catalytic Pt atoms are geometrically isolated by inactive In atoms which completely eliminates Pt 3-fold hollow sites necessary for ethylidyne formation. Although the bulk stoichiometry and structure are different, the local coordination environment of Pt in $PtIn_2$ is equivalent to Pd in the 1:1 PdZn and PdIn alloys where high dehydrogenation selectivity was attributed to the isolation of Pd atoms by the inactive metal [21–23]. Accordingly, the isolated Pt atoms in Pt–In(1.4) are highly selective for dehydrogenation reactions.

Accompanying the geometric changes of alloy formation are concomitant electronic changes to Pt which are likely responsible for the increases seen in the TORs and E_{app} of the Pt–In catalysts. XPS and XANES studies on bimetallic Pt–Sn catalysts have shown that the

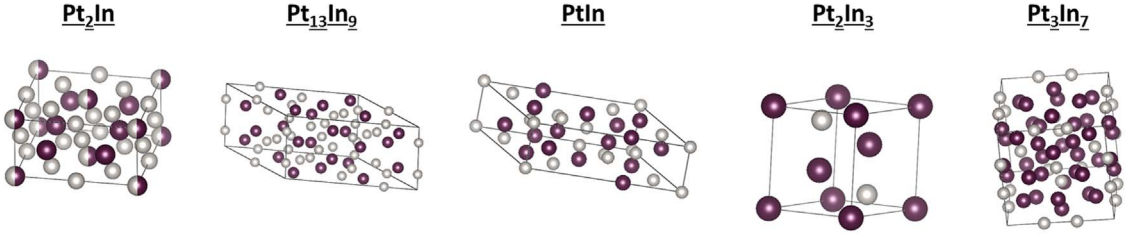

Fig. 6. Crystal structures of Pt–In intermetallic alloys not formed in the Pt–In catalysts (Pt - light atoms and In - dark atoms.) [41–45].

electronic properties of Pt are altered by interactions with Sn. The binding energy of Pt $4f_{7/2}$ electrons as measured by XPS has been reported to decrease while the Pt L_{III} XANES energy has been reported to increase [20,55]. It has been proposed that these changes are due to a d → s, p rehybridization that occurs upon formation of Pt–Sn bonds resulting in a decrease in the occupancy of the Pt 5d orbitals [20,55–57]. However, this would yield no change in the XANES energy and an increase in the white line intensity.

For the bimetallic catalysts the Pt L_{III} XANES energy increases and the white line intensity decreases. The increase in XANES energy indicates an upward shift in the unfilled valance states of Pt while the decrease in the white line intensity suggests higher occupancy of the 5d orbitals. Molecular Orbital (MO) Theory would predict that the formation of Pt–In bonds would result in new filled bonding and unfilled anti-bonding state in Pt. A shift to higher energy in the PtIn XANES spectra suggests that the energy of the empty 5d orbitals are at higher energy compared to Pt. From MO Theory, this also implies Pt–In bond formation results in the filled 5d orbitals in Pt being lower in energy. A shift to lower energy would result in less hybridization of the 5d with the 6s and 6p orbitals leading to higher electron density in the 5d states and a decrease in the white line intensity. The effects of rehybridization on white line intensity are well documented for changes in size of metal clusters [34,58–60]. Changes in the 5d states likely modify the adsorption of reactants and products leading to changes in catalytic performance. Electronic changes are also evident from the increases in the apparent activation energy, a convolution of heat of adsorption and intrinsic activation energy, seen for the Pt–In catalysts. Experimental and theoretical results on Pt–Sn surfaces have shown that alloy formation reduces the binding strengths of alkenes to Pt [3,4,51]. It is possible that the formation of Pt–In alloys leads to weaker adsorption of alkenes, resulting in faster ethylene desorption and promoting dehydrogenation TORs, similar to what has been proposed for Pt–Sn catalysts.

5. Conclusions

The addition of In to Pt catalysts leads to the formation of intermetallic alloy nanoparticles. At an In:Pt atomic ratio of 0.7 the Pt_3In phase with a Cu_3Au structure formed. A shell of $PtIn_2$ with a CaF_2 structure forms around a core of Pt_3In when the In:Pt ratio is increased to 1.4. The Pt_3In and $PtIn_2$ alloys are structurally similar to FCC Pt and their formation requires minimal atomic rearrangement when compared to phases not observed suggesting alloy formation is kinetically controlled. When compared to a monometallic Pt catalyst the intermetallic alloys exhibited superior performance for ethane dehydrogenation, i.e. higher ethylene selectivity and turnover rates. The increase in selectivity to nearly 100% can be attributed to geometric changes to the catalytic Pt atoms. Ensembles responsible for structure sensitive hydrogenolysis reactions are eliminated upon alloy formation; while structure insensitive dehydrogenation, which requires a single active site, is unaffected. The increases in TOR are likely due to electronic changes to Pt arising from the formation of Pt–In bonds. Further studies are necessary to fully understand the electronic properties of Pt intermetallic alloy nanoparticles. This work shows that it is possible to tailor both the geometric and electronic properties of catalysts by synthesizing intermetallic alloy nanoparticles of different stoichiometry's and structures.

Acknowledgements

Financial support was provided by the Davidson School of Chemical Engineering, Purdue University. The authors acknowledge the use of the Electron Microscopy facility at Birck Nanotechnology Center, Purdue University, support for which was provided by a Kirk Endowment Exploratory Research Recharge Grant. Use of the Advanced Photon Source was supported by the U.S. Department of Energy, Office of Basic Energy Sciences, under contract no. DE-AC02-06CH11357. MRCAT operations are supported by the Department of Energy and MRCAT member institutions. The authors acknowledge the use of the 10-BM and 11-ID-C beamlines at the APS.

References

[1] J.J. Siirola, AIChE J. 60 (2014) 810–819.
[2] J.J. Sattler, J. Ruiz-Martinez, E. Santillan-Jimenez, B.M. Weckhuysen, Chem. Rev. 114 (2014) 10613–10653.
[3] R.D. Cortright, J.A. Dumesic, J. Catal. 148 (1994) 771–778.
[4] R.D. Cortright, J.M. Hill, J.A. Dumesic, Catal. Today 55 (2000) 213–223.
[5] V. Galvita, G. Siddiqi, P. Sun, A.T. Bell, J. Catal. 271 (2010) 209–219.
[6] D. Sanfilippo, I. Miracca, Catal. Today 111 (2006) 133–139.
[7] D. Akporiaye, S.F. Jensen, U. Olsbye, F. Rohr, E. Rytter, M. Rønnekleiv, A.I. Spjelkavik, Ind. Eng. Chem. Res. 40 (2001) 4741–4748.
[8] O.A. Bariås, A. Holmen, E.A. Blekkan, J. Catal. 158 (1996) 1–12.
[9] A. Virnovskaia, S. Morandi, E. Rytter, G. Ghiotti, U. Olsbye, J. Phys. Chem. C 111 (2007) 14732–14742.
[10] L. Bednarova, C.E. Lyman, E. Rytter, A. Holman, J. Catal. 211 (2002) 335–346.
[11] N. Nava, P. Del Angel, J. Salmones, E. Baggio-Saitovitch, P. Santiago, Appl. Surf. Sci. 253 (2007) 9215–9220.
[12] J. Llorca, N. Homs, J. León, J. Sales, J.L.G. Fierro, P. Ramirez de la Piscina, Appl. Catal. A: Gen. 189 (1999) 77–86.
[13] J. Llorca, N. Homs, J.L.G. Fierro, J. Sales, P. Ramirez de la Piscina, J. Catal. 166 (1997) 44–52.
[14] B.K. Vu, M.B. Song, I.Y. Ahn, Y. Suh, D.J. Suh, W. Kim, H. Koh, Y.G. Choi, E.W. Shin, Catal. Today 164 (2011) 214–220.
[15] L. Deng, T. Shishido, K. Teramura, T. Tanaka, Catal. Today 232 (2014) 33–39.
[16] R. Srinivasan, R. Sharma, S. Su, B. Davis, Catal. Today 21 (1994) 83–99.
[17] L. Deng, H. Miura, T. Shishido, S. Hosokawa, K. Teramura, T. Tanaka, ChemCatChem 6 (2014) 2680–2691.
[18] M. Yang, Y. Zhu, X. Zhou, Z. Sui, D. Chen, ACS Catal. 2 (2012) 1247–1258.
[19] J. Ruiz-Martínez, A. Sepúlveda-Escribano, J.A. Anderson, F. Rodríguez-Reinoso, Catal. Today 123 (2007) 235–244.
[20] G.J. Siri, J.M. Ramallo-López, M.L. Casella, J.L.G. Fierro, F.G. Requejo, O.A. Ferretti, Appl. Catal. A: Gen. 278 (2005) 239–249.
[21] D.J. Childers, N.M. Schweitzer, S. Mehdi Kamali Shahari, R.M. Rioux, J.T. Miller, R.J. Meyer, J. Catal. 318 (2014) 75–84.
[22] J.R. Gallagher, D.J. Childers, H. Zhao, R.E. Winans, R.J. Meyer, J.T. Miller, Phys. Chem. Chem. Phys. 17 (2015) 28144–28153.
[23] Z. Wu, E.C. Wegener, H. Tseng, J.R. Gallagher, J.W. Harris, R.E. Diaz, Y. Ren, F.H. Ribeiro, J.T. Miller, Catal. Sci. Technol. 6 (2016) 6965–6976.
[24] P. Sun, G. Siddiq, W.C. Vining, M. Chi, A.T. Bell, J. Catal. 282 (2011) 165–174.
[25] P. Mériaudeau, C. Naccache, A. Thangaraj, C.L. Bianchi, R. Carli, S. Narayanan, J. Catal. 152 (1995) 313–321.
[26] P. Mériaudeau, A. Thangaraj, J.F. Dutel, P. Gelin, C. Naccache, J. Catal. 163 (1996) 338–345.
[27] H. Okamoto, J. Phase Equilib. Diffus. 26 (2005) 399.
[28] M. Armbrüster, R. Schlögl, Y. Grin, Sci. Technol. Adv. Mater. 15 (2014) 1–17.
[29] T. Ressler, J. Synchrotr. Radiat. 5 (1998) 118–122.
[30] J.J. Rehr, R.C. Albers, Rev. Mod. Phys. 72 (2000) 621–654.
[31] A. Hammersley, S. Svensson, M. Hanfland, A. Fitch, D. Hausermann, Int. J. High Press. Res. 14 (1996) 235–248.
[32] L. Lutterotti, S. Matthies, H. Wenk, IUCr: Newsletter of the CPD 21 (1999).
[33] N.A. Koryabkina, A.A. Phatak, W.F. Ruettinger, R.J. Farrauto, F.H. Ribeiro, J. Catal. 217 (2003) 233–239.
[34] J.T. Miller, A.J. Kropf, Y. Zha, J.R. Regalbuto, L. Delannoy, C. Louis, E. Bus, J.A. van Bokhoven, J. Catal. 240 (2006) 222–234.
[35] D.B. Buchholz, Q. Ma, D. Alducin, A. Ponce, M. Jose-Yacaman, R. Khanal, J.E. Medvedeva, R.P.H. Chang, Chem. Mater. 26 (2014) 5401–5411.
[36] J.R. Gallagher, T. Li, H. Zhao, J. Liu, Y. Lei, X. Zhang, Y. Ren, J.W. Elam, R.J. Meyer, R.E. Winans, J.T. Miller, Catal. Sci. Technol. 4 (2014) 3053–3063.
[37] H.E. Swanson, E. Tatge, Natl. Bur. Stand. (U.S.) 539 (1953) 95.
[38] Z. Yu, Acta Geol. Sin. 71 (1997) 480–485.
[39] H. Okamoto, II ed., T.B. Massalski (Ed.), Binary Alloy Phase Diagrams, vol. 3, 1990, pp. 3068–3070.
[40] H. Okamoto, J. Phase Equilib. 24 (2003) 481.
[41] S. Bhan, K. Schubert, J. Less-Comm. Metals 17 (1969) 73–90.
[42] M. Ellner, S. Bhan, K. Schubert, J. Less-Comm. Metals 19 (1969) 245–252.
[43] S. Heinrich, K. Schubert, J. Less-Comm. Metals 57 (1978) 1–7.
[44] K.C. Jain, S. Bhan, Trans. Ind. Inst. Metals 25 (1972) 100–102.
[45] H.A. Friedrch, J. Koehler, Zeit. Kristallogr. – New Cryst. Struct. 217 (2002) 24.
[46] P. Biloen, F.M. Dautzenberg, W.M.H. Sachtler, J. Catal. 50 (1977) 77–86.
[47] M. Boudart, J. Mol. Catal. 30 (1985) 27–38.
[48] Y. Tsai, B.E. Koel, J. Phys. Chem. B 101 (1997) 2895–2906.
[49] Z. Nomikou, M.A. Van Hove, G.A. Somorjai, Langmuir 12 (1996) 1251–1256.
[50] J. Shen, J.M. Hill, R.M. Watwe, B.E. Spiewak, J.A. Dumesic, J. Phys. Chem. B 103 (1999) 3923–3934.
[51] R.M. Watwe, R.D. Cortright, M. Mavrikakis, J.K. Nørskov, J.A. Dumesic, J. Chem. Phys. 114 (2000) 4663–4668.
[52] S.A. Goddard, M.D. Amiridis, J.E. Rekoske, N. Cardona-Martinez, J.A. Dumesic, J. Catal. 117 (1989) 155–169.
[53] G.A. Martin, J. Catal. 60 (1979) 345–355.

[54] D.W. Flaherty, E. Iglesia, J. Am. Chem. Soc. 135 (2013) 18586–18599.
[55] J.M. Ramallo-López, G.F. Santori, L. Giovanetti, M.L. Casella, O.A. Ferretti, F.G. Requejo, J. Phys. Chem. B 107 (2003) 11441–11451.
[56] J.A. Rodriguez, S. Chaturvedi, T. Jirsak, J. Hrbek, J. Chem. Phys. 109 (1998) 4052–4062.
[57] J.A. Rodriguez, T. Jirsak, S. Chaturvedi, J. Hrbek, J. Am. Chem. Soc. 120 (1998) 11149–11157.
[58] M.G. Mason, Phys. Rev. B 27 (1983) 748–762.
[59] L.F. Mattheiss, R.E. Dietz, Phys. Rev. B 22 (1980) 1663–1676.
[60] P.K. Jain, Struct. Chem. 16 (2005) 421–426.